Angular Momentum Transport and Particle Acceleration During Magnetorotational Instability in a Kinetic Accretion Disk

Masahiro Hoshino*
Department of Earth and Planetary Science, University of Tokyo, Tokyo 113-0033, Japan
(Received 28 September 2014; published 12 February 2015)

Angular momentum transport and particle acceleration during the magnetorotational instability (MRI) in a collisionless accretion disk are investigated using three-dimensional particle-in-cell simulation. We show that the kinetic MRI can provide not only high-energy particle acceleration but also enhancement of angular momentum transport. We find that the plasma pressure anisotropy inside the channel flow with $p_\parallel > p_\perp$ induced by active magnetic reconnection suppresses the onset of subsequent reconnection, which, in turn, leads to high-magnetic-field saturation and enhancement of the Maxwell stress tensor of angular momentum transport. Meanwhile, during the quiescent stage of reconnection, the plasma isotropization progresses in the channel flow and the anisotropic plasma with $p_\perp > p_\parallel$ due to the dynamo action of MRI outside the channel flow contribute to rapid reconnection and strong particle acceleration. This efficient particle acceleration and enhanced angular momentum transport in a collisionless accretion disk may explain the origin of high-energy particles observed around massive black holes.

DOI: 10.1103/PhysRevLett.114.061101 PACS numbers: 95.30.Qd, 52.35.Vd, 52.65.Rr, 97.10.Gz

A fundamental obstacle in our understanding of the Universe is the need to explain the angular momentum redistribution in an accretion disk gravitationally rotating around a central object. It has been proposed that magnetorotational instability (MRI) is the most efficient mechanism for transporting angular momentum outward with inward mass motion [1,2]. Based on magnetohydrodynamic (MHD) simulations (e.g., Refs. [3–7]), it has been asserted that a weakly magnetized disk with an outwardly decreasing angular velocity gradient can provide angular momentum transport at a greatly enhanced rate by generating MHD turbulence.

While the MHD framework is successful in explaining the "collisional" accretion disks, it is also important to study the dynamnics of "collisionless" accretion disks for some classes of astrophysical objects [8]. The accretion disk around the supermassive black hole Sagittarius A* at the center of our Galaxy is believed to be in a collisionless plasma state. This is because the accretion proceeds through a hot and low-density plasma in which the proton temperature is higher than the electron temperature (e.g., Ref. [9]). In addition to the nonequilibrium temperature between protons and electrons, nonthermal high-energy particles are observed (e.g., Refs. [10–13]).

Motivated by the observation of this collisionless accretion disk, Sharma *et al.*. [14,15] studied the MRI, including the effect of pressure anisotropy. Since the MRI involves the process of magnetic field amplification or dynamo, the perpendicular pressure is expected to be enhanced in the double adiabatic approximation [16], which, in turn, modifies the MHD wave behavior. Meanwhile, because of the MHD waves generated by pressure anisotropy instabilities (e.g., Ref. [17]), pressure isotropization occurs during MRI evolution. Riquelme *et al.* [18] and Hoshino [19] performed two-dimensional particle-in-cell (PIC) simulations and confirmed the excitation of the mirror mode and the relaxation of pressure anisotropy studied by the previous fluid-based model [15]. In addition to the pressure anisotropy effect, the formation of a power-law energy spectrum during magnetic reconnection was pointed out.

Although the previous two-dimensional PIC simulation showed the importance of the kinetic accretion disk, the plasma transport process is generally different depending on whether it is considered in two-dimensional or three-dimensional space. The most important determinant of the efficiency of angular momentum transport in the collisionless MRI remains an open question. In this Letter, we investigate for the first time the collisionless MRI using a three-dimensional PIC simulation and argue that the angular momentum transport can be enhanced by the pressure anisotropy.

To study the kinetic accretion disk in three-dimensional space, we performed a PIC simulation in a local frame rotating with angular velocity $\Omega_0 \vec{e}_z$ at a distance r_0 from the central object, and we include Coriolis, centrifugal, and gravitational forces in the equations of motion. We used tidal expansion of the effective potential with a constant $q = -\partial \ln \Omega / \partial \ln r$ at r_0, where q is $3/2$ for a Keplerian disk. The equation of motion becomes

$$\frac{d\vec{p}}{dt} = e\left(\vec{E} + \frac{\vec{v}}{c} \times \vec{B}\right) - m\gamma(2\vec{\Omega}_0 \times \vec{v} - 2q\Omega_0^2 x \vec{e}_x). \quad (1)$$

Our scheme was the same as that used in our previous two-dimensional MRI study, and we assumed that the local rotating velocity $\Omega_0 r_0$ is much smaller than the speed of

light [19]. We adopted the shearing box boundary condition established by MHD simulations [20].

For the initial condition, a drifting Maxwellian velocity distribution function was assumed in the local rotating frame with angular velocity $\Omega_0(r_0)$. The drift velocity in the y direction $v_y(x)$ was given by $v_y(x) = r\Omega(r) - r\Omega_0(r_0) \simeq -q\Omega_0(r_0)x$, and the radial velocity v_x and the vertical velocity v_z were both zero. In order to save CPU time, we set up the pair plasma, but the linear behavior of the MRI in the pair plasma was the same as that of ion-electron plasmas [19]. A nonrelativistic isotropic plasma pressure with a high plasma $\beta = 8\pi(p_+ + p_-)/B_0^2 = 1536$ was assumed, where the electron and positron gas pressures were related to the thermal velocities $v_{t\pm}$ by $p_\pm = (3/2)m_\pm n v_{t\pm}^2$. The initial magnetic field was oriented purely vertical to the accretion disk, i.e., $\vec{B} = (0, 0, B_0)$. The ratio of the cyclotron frequency to the disk angular velocity was fixed at $\Omega_{c\pm}/\Omega_0 = \pm 10$, where $\Omega_{c\pm} = e_\pm B_0/m_\pm c$. The grid size Δ was set to $2^{3/2}(v_{t\pm}/\Omega_{p\pm})$, where $\Omega_{p\pm} = \sqrt{8\pi n e^2/m_\pm}$ is the pair plasma frequency. The Alfvén velocity is defined as $V_A = B/\sqrt{8\pi m_\pm n}$, so that the plasma β is equal to $3v_{t\pm}^2/V_A^2$. The parameters used were $(V_A/\Omega_0)/\Delta = 25$, $(v_{t\pm}/\Omega_{c\pm})/\Delta = 56.4$, $V_A/c = 6.25 \times 10^{-3}$. N_x, N_y, and N_z are the grid sizes in the x, y, and z directions, respectively, and we assumed $N_x = N_z = N_z = 300$ in this Letter. $L_x = L_y = L_z = (N_x\Delta)/\lambda = 1.91$ is the physical size normalized by $\lambda = 2\pi V_A/\Omega_0$. The number of particles per cell was set to $N_p/\text{cell} = 40$.

Figure 1 shows the time evolution of the magnetic field lines (greenish lines) and the structure of the high-density regions (sandwiched by the reddish curved planes). Color contours in the background at $Y = 1.91$ and $X = 1.91$ show the angular velocity v_y in the local rotating frame. In the early stage at $T_{\text{orbit}} = \Omega_0 t/2\pi = 0.31$ in Fig. 1(a), the magnetic field lines are parallel to the z axis, and the Keplerian motion or differential motion of v_y can be seen as the color contour at $Y = 1.91$, where the reddish (bluish) region corresponds to a positive (negative) toroidal velocity. As time passes, the vertical magnetic fields start to get distorted due to the MRI, and they are stretched out in the toroidal direction because of the Keplerian motion at $T_{\text{orbit}} = 6.89$ in Fig. 1(b). This stretching motion can amplify the magnetic field and form two inward- and outward-flowing streams with a high plasma density and strong electric current called the channel flow. The reddish regions sandwiched by two surfaces in Fig. 1(c) show the high-density channel flow with $\rho \geq \langle\rho\rangle + 2\sigma_\rho$ where $\langle\rho\rangle$ and σ_ρ are the average density and standard deviation of density distribution in the simulation domain, respectively.

The amplification of the magnetic field stretched by the Keplerian motion may be balanced by the magnetic field

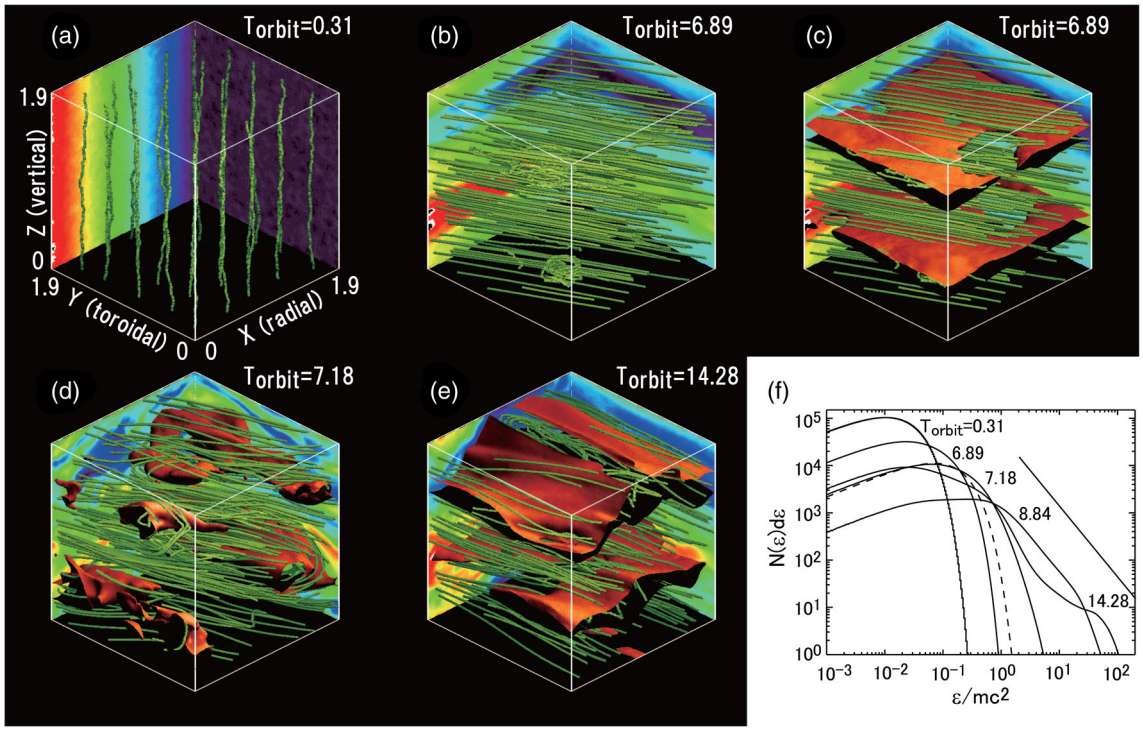

FIG. 1 (color online). Time evolution of the magnetorotational instability. Panels (a) and (b) show the magnetic field lines (greenish lines) and angular velocities in the background at $Y = y/\lambda = 1.91$ and $X = x/\lambda = 1.91$ (color contour), and panels (c)–(e) depict the high-density regions as reddish curved planes. Panels (b) and (c) are at the same time stage. Panel (f): The energy spectra during the MRI at $T_{\text{orbit}} = 0.31$, 6.89, 7.18, 8.84, and 14.28. The dashed line is a Maxwellian fitting for $T_{\text{orbit}} = 7.18$.

dissipation caused by magnetic reconnection. Figure 1(d) at $T_{\rm orbit} = 7.18$ is the stage just after the onset of magnetic reconnection, and the break of the laminar channel flow seen at $T_{\rm orbit} = 6.89$ can be observed. After the first onset of reconnection, subsequent reconnection occurs intermittently in several different sites in the turbulent channel flows, and the formation of the channel flow with a strong magnetic field by MRI dynamo and destruction by reconnection occurs repeatedly.

Figure 1(f) shows the time evolution of the energy spectra, where the horizontal and vertical axes are the particle energy normalized by the rest mass energy and number density $N(\varepsilon)$. Before the first onset of magnetic reconnection at $T_{\rm orbit} = 6.89$, the plasmas are gradually heated from the initial cold Maxwellian plasma. After the onset of reconnection at $T_{\rm orbit} = 7.18$, we can clearly observe nonthermal particles above $\varepsilon/mc^2 > 0.2$. The dashed line, for reference, is a Maxwellian spectrum fitted by $T/mc^2 = 0.121$. The nonthermal population continues to grow, and the spectrum can be approximated by a single power-law function with $N(\varepsilon) \propto \varepsilon^{-3/2}$ at $T_{\rm orbit} = 8.84$. After $T_{\rm orbit} = 9 \sim 10$, the spectrum slope becomes harder in the high-energy range from $\varepsilon/mc^2 \sim 10$ to 10^2. The spectrum hardening might be due to the stochastic multiple reconnection process [21], but note that the maximum attainable energy in the system, whose gyroradius is almost the same as the simulation box size, is $\varepsilon/mc^2 \sim 10^2$. Then the spectrum deformation might be related to the accumulation of high-energy particles around the maximum attainable energy. As already discussed by the previous 2D PIC simulations [18,19], the pressure anisotropy with $p_\perp > p_\parallel$ is generated in our 3D simulation by the MRI dynamo (see Fig. 3), which can contribute to rapid reconnection [22] and particle acceleration [19].

Let us take a look at the history of kinetic and magnetic field energies in the top panel of Fig. 2. The energies are normalized by the initial magnetic field energy. As time goes on, both the kinetic and magnetic field energies increase, but the rapid increase of the magnetic field energy can be observed at around $T_{\rm orbit} \sim 6$, and the instantaneous plasma β becomes of the order of unity. Our PIC simulation in the local rotating system has been carried out using the open shearing box boundary condition [20], and the plasmas can acquire their energies by accretion toward the center of gravity. Around $T_{\rm orbit} \sim 8$, the total magnetic field energy reaches to its maximum and then starts to decrease until $T_{\rm orbit} \sim 9$. After $T_{\rm orbit} \sim 9$, both the magnetic field and kinetic energies remain almost constant with fluctuations.

This time evolution is basically similar to our previous 2D PIC simulation result [19]. In the early nonlinear stage, we observe the formation of channel flows with the amplification of the magnetic field and the subsequent break of the channel flow by reconnection. The main difference, however, is seen in the late nonlinear stage with the turbulent or intermittent reconnection after $T_{\rm orbit} \geq 9$. In our previous 2D simulation, after the first onset of reconnection, the channel flows are destroyed, and a couple of large magnetic islands are formed in the system. In this 3D simulation, however, the channel flows are preserved beyond the first onset of reconnection, and magnetic reconnection occurs in several different locations with the dynamic motion. The turbulent or intermittent reconnection in the late phase can be seen in 3D MHD simulations as well [3–7].

The most intriguing result in our kinetic MRI simulation is the enhancement of the angular momentum transport. The bottom panel in Fig. 2 shows the time evolution of parameter α, which is used in the standard accretion disk model [23] and can be defined as $\alpha = w_{xy}/p$, where p and w_{xy} are the volume-averaged, instantaneous plasma pressure, and stress tensor, respectively. The stress tensor w_{xy}, which is related to the energy dissipation rate in the system, can be calculated as follows:

$$w_{xy} = \rho v_x (v_y + q\Omega_0 x) - \frac{B_x B_y}{4\pi} + \frac{(p_\parallel - p_\perp)}{B^2} B_x B_y. \quad (2)$$

The terms on the right-hand side represent the Reynolds (w_R), Maxwell (w_M), and anisotropy (w_A) stresses, respectively [15]. During the active reconnection phase between $7 < T_{\rm orbit} < 9$, we found that α reached $O(1)$ with $w_M > w_R \sim w_A$, and during the late stage of $T_{\rm orbit} > 9$, $\alpha \sim O(10^{-1})$ with $w_M \sim w_A > w_R$, which suggests a much more efficient angular momentum transport than the one discussed previously with $\alpha \sim O(10^{-3}$–$10^{-2})$ [6,20]. Note that α in some simulation results was normalized by

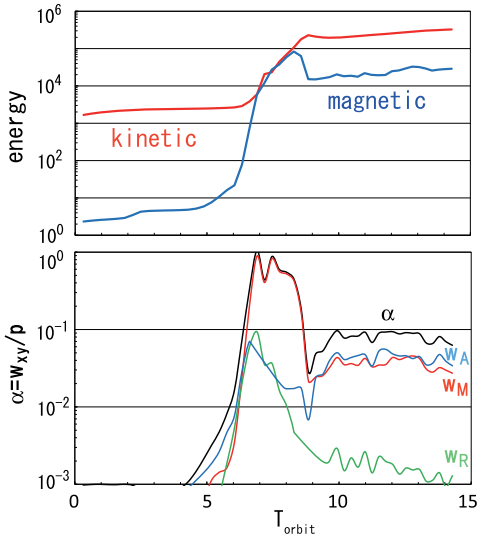

FIG. 2 (color online). (Top) Time evolution of the kinetic and magnetic field energies. (Bottom) The α parameter (black) and the contribution of Reynolds stress w_R/p (green), Maxwell stress w_M/p (red), and anisotropy stress w_A/p (blue).

the initial pressure p_0 instead of the instantaneous pressure p.

Since the parameter α is approximated by

$$\alpha = \frac{w_{xy}}{p} \sim \left(-\frac{2B_x B_y}{B^2}\right)\left(\frac{B^2/8\pi}{p}\right) \sim \frac{1}{\beta}, \tag{3}$$

the enhancement of parameter α is related to a higher saturation of the magnetic field, which can be determined from the balance between the magnetic field amplification due to the MRI dynamo and magnetic field dissipation by reconnection. The dissipated magnetic field energy is deposited as thermal energy. If the onset of reconnection requires a high magnetic field in the collisionless system, then the plasma β becomes small and a large α can be realized.

To understand the dynamics of reconnection, we focus on the pressure anisotropy. Figures 3(a) and 3(b) at $T_{\rm orbit} = 14.28$ show, respectively, two-dimensional (x, z) slices of plasma density and pressure anisotropy $p_\perp/p_\parallel$ at the position $Y = 0.96$. The higher density regions around $Z = 0.64$ and 1.60 correspond to the so-called channel flows where the magnetic field polarity changes. At the center of the channel flow, one can see $p_\perp/p_\parallel \leq 1$, while $p_\perp/p_\parallel > 1$ for the other regions. Figure 3(c) shows the relationship between the plasma density and $p_\perp/p_\parallel$, and Fig. 3(d) is the histogram of occurrence frequency. This behavior can be basically understood using the double adiabatic equation of state with $p_\perp/\rho B = \text{const}$ and $p_\parallel B^2/\rho^3 = \text{const}$ [15,18,19]. The production of $p_\perp/p_\parallel > 1$ is simply due to the magnetic field amplification of the MRI dynamo, and the formation of $p_\parallel/p_\perp > 1$ is because of magnetic reconnection at the center of the channel flow, where the total B is dissipated while the plasma density is compressed. In the kinetic perspective, it is known that the pressure anisotropy can be produced by the Alfvénic beams along the plasma sheet boundary, which are emanating from the magnetic diffusion region [24].

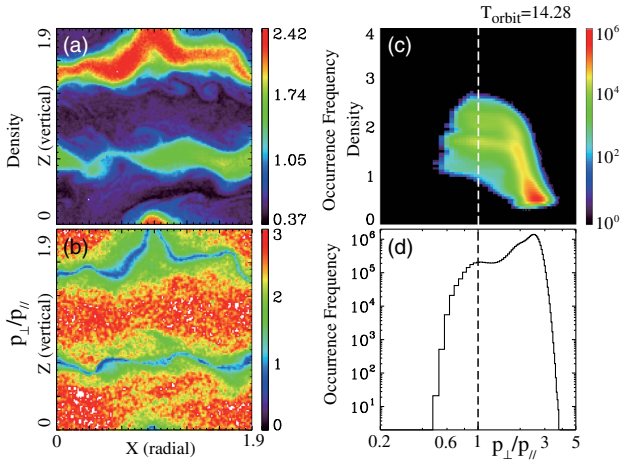

FIG. 3 (color online). (a) A slice of the three-dimensional density in the x-z plane at $Y = 0.96$ and (b) a slice of the pressure anisotropy $p_\perp/p_\parallel$ in the same plane. The color scales are shown on the right. (c) The color contour of the occurrence frequency in the $(\rho, p_\perp/p_\parallel)$ plane, and (d) the histogram of the occurrence frequency as a function of $p_\perp/p_\parallel$ in the logarithmic scale.

The onset of magnetic reconnection is still a controversial issue, but the linear growth rate of the collisionless tearing mode under the pressure anisotropy would be sufficient for our argument. This is given, for example, by simplifying Eq. (40) in Ref. [22], as follows:

$$\frac{\mathrm{Im}(\omega)}{k v_{\rm th}} \simeq \left(\frac{p_\perp}{p_\parallel} - 1\right) + \left(\frac{r_g}{\delta}\right)^{3/2}\left(\frac{1 - k^2\delta^2}{k\delta}\right), \tag{4}$$

where k, δ, r_g, and $v_{\rm th}$ are the wave number, the thickness of the current sheet, gyroradius, and thermal velocity, respectively. At the saturation stage, $v_{\rm th} \leq c$, $B/B_0 \sim 230$, and $\delta/\Delta \geq 10$. We then obtain the estimates of $(r_g/\delta)^{3/2} \leq 0.089$ and $(1 - k^2\delta^2)/k\delta \sim O(1)$. On the other hand, the pressure anisotropy is $1 - p_\perp/p_\parallel < 0.5$ from Fig. 3(d). Therefore, it is highly possible that the successive reconnection in the channel flow is suppressed by anisotropic plasma of $p_\perp/p_\parallel < 1$, which is formed by the preceding reconnection. The kinetic magnetic reconnection involves a deterrent effect to the successive magnetic dissipation, and as a result, the high magnetic field is realized before the onset of reconnection.

To confirm the enhancement of the α parameter by the $p_\parallel > p_\perp$ effect in the channel flow, we performed another simulation including an isotropization model for an anisotropic plasma after the formation of the channel flow, $T_{\rm orbit} > 6.89$. In this model, we added a weak external random magnetic field $\delta\vec{B}$ in Eq. (1) only for the channel flow region, which is roughly characterized by the weak magnetic field region of $|B/B_0| < 50$. Namely, we used the motion of equation given by

$$\frac{d\vec{p}}{dt} = e\left(\vec{E} + \frac{\vec{v}}{c} \times (\vec{B} + \delta\vec{B})\right) + (\text{other forces}), \tag{5}$$

where we assumed the white noise δB with $|\delta B|/|B| = 2.5$.

Shown in the top panel of Fig. 4 is the time history of the volume-integrated pressure anisotropy $p_\perp/p_\parallel$. The dashed and solid lines correspond to the cases with and without the above isotropization model, respectively. As we expected, one can find that the $p_\perp/p_\parallel$ with the isotropization model in the channel flow is larger than that without the isotropization, because the anisotropic plasma with $p_\parallel > p_\perp$ in the channel flow can be reduced by the isotropization model.

Under this weak isotropization in the channel flow, let us study the time history of the α parameter and the Reynolds

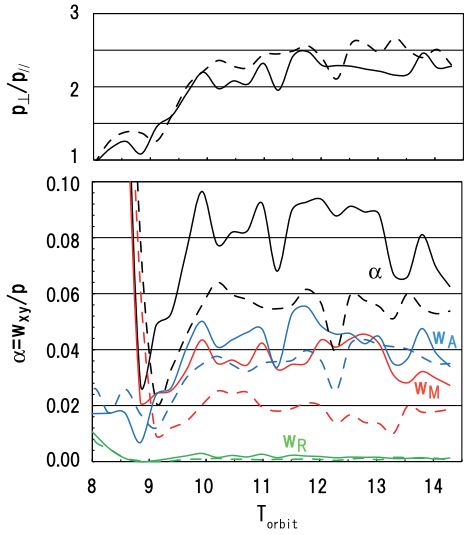

FIG. 4 (color online). (Top) Time evolution of the volume-integrated pressure anisotropy. The dashed and solid lines show the cases with and without the isotropization model, respectively. (Bottom) The α parameter (black) and the contribution of Reynolds stress w_R/p (green), Maxwell stress w_M/p (red), and anisotropy stress w_A/p (blue).

w_R/p, Maxwell w_M/p, and anisotropy stress w_A/p with and without the isotropization model in the bottom panel. The dashed and solid lines show the cases with and without the isotropization model, respectively. One can find that the α parameter can be reduced under the isotropization model. The magnitude of the anisotropy stress w_A/p does not change between the two cases with and without the isotropization model, while the change of the Maxwell stress w_M/p becomes large under the isotropization model. This suggests that the isotropization in the channel flow plays an important role in the magnetic field generation during the MRI dynamo.

In summary, we have investigated for the first time a three-dimensional collisionless MRI in a local rotating system and have shown that an anisotropic pressure of $p_\parallel/p_\perp > 1$ is maintained in the channel flow during the MRI, which leads to high-magnetic-field saturation and an enhanced α parameter. During the quiescent stage of reconnection, the isotropization of the anisotropic plasma progresses in the channel flow. After the plasma isotropization, the anisotropic plasma with $p_\perp/p_\parallel > 1$ outside the channel flow region may contribute to a rapid reconnection and nonthermal particle generation [19].

This work was supported by JSPS Grant-in-Aid for Scientific Research (KAKENHI) Grant No. 25287151.

*hoshino@eps.s.u-tokyo.ac.jp

[1] S. A. Balbus and J. F. Hawley, Astrophys. J. **376**, 214 (1991).
[2] S. A. Balbus and J. F. Hawley, Rev. Mod. Phys. **70**, 1 (1998).
[3] J. F. Hawley and S. A. Balbus, Astrophys. J. **376**, 223 (1991).
[4] J. F. Hawley and S. A. Balbus, Astrophys. J. **400**, 595 (1992).
[5] R. Matsumoto and T. Tajima, Astrophys. J. **445**, 767 (1995).
[6] T. Sano, S.-I. Inutsuka, N. J. Turner, and J. M. Stone, Astrophys. J. **605**, 321 (2004).
[7] J. M. Stone, J. F. Hawley, C. F. Gammie, and S. A. Balbus, Astrophys. J. **463**, 656 (1996).
[8] E. Quataert, W. Dorland, and G. W. Hammett, Astrophys. J. **577**, 524 (2002).
[9] R. Narayan, R. Mahadevan, and E. Quataert, in *Theory of Black Hole Accretion Disks*, edited by M. A. Abramowicz, G. Bjornsson, and J. E. Pringle (Cambridge University Press, Cambridge, England, 1998), p. 148.
[10] F. Yuan, E. Quataert, and R. Narayan, Astrophys. J. **598**, 301 (2003).
[11] F. Aharonian, J. Buckley, T. Kifune, and G. Sinnis, Rep. Prog. Phys. **71**, 096901 (2008).
[12] M. Chernyakova, D. Malyshev, F. A. Aharonian, R. M. Crocker, and D. I. Jones, Astrophys. J. **726**, 60 (2011).
[13] M. Kusunose and F. Takahara, Astrophys. J. **748**, 34 (2012).
[14] P. Sharma, G. W. Hammett, and E. Quataert, Astrophys. J. **596**, 1121 (2003).
[15] P. Sharma, G. W. Hammett, E. Quataert, and J. M. Stone, Astrophys. J. **637**, 952 (2006).
[16] G. F. Chew, M. L. Goldberger, and F. E. Low, Proc. R. Soc. A **236**, 112 (1956).
[17] S. P. Gary, J. Wang, D. Winske, and S. A. Fuselier, J. Geophys. Res. **102**, 27159 (1997).
[18] M. A. Riquelme, E. Quataert, P. Sharma, and A. Spitkovsky, Astrophys. J. **755**, 50 (2012).
[19] M. Hoshino, Astrophys. J. **773**, 118 (2013).
[20] J. F. Hawley, C. F. Gammie, and S. A. Balbus, Astrophys. J. **440**, 742 (1995).
[21] M. Hoshino, Phys. Rev. Lett. **108**, 135003 (2012).
[22] J. Chen and P. Palmadesso, Phys. Fluids **27**, 1198 (1984).
[23] N. I. Shakura and R. A. Sunyaev, Astron. Astrophys. **24**, 337 (1973).
[24] M. Hoshino, T. Mukai, T. Yamamoto, and S. Kokubun, J. Geophys. Res. **103**, 4509 (1998).